

Probing early-time longitudinal dynamics with the Λ hyperon's spin polarization in relativistic heavy-ion collisions

Sangwook Ryu,^{1,*} Vahidin Jopic,^{1,†} and Chun Shen^{1,2,‡}

¹*Department of Physics and Astronomy, Wayne State University, Detroit, Michigan 48201, USA*

²*RIKEN BNL Research Center, Brookhaven National Laboratory, Upton, New York 11973, USA*



(Received 24 June 2021; accepted 14 September 2021; published 23 November 2021)

We systematically study the hyperon global polarization's sensitivity to a collision system's initial longitudinal flow velocity in hydrodynamic simulations. By explicitly imposing local energy-momentum conservation when mapping the initial collision geometry to macroscopic hydrodynamic fields, we study the evolution of the system's orbital angular momentum (OAM) and fluid vorticity. We find that a simultaneous description of the Λ hyperon's global polarization and the slope of the pion's directed flow can strongly constrain the size of longitudinal flow at the beginning of hydrodynamic evolution. We extract the size of the initial longitudinal flow and the fraction of orbital angular momentum in the produced quark-gluon plasma fluid as a function of collision energy with the STAR measurements in the Beam Energy Scan program at the BNL Relativistic Heavy-Ion Collider. We find that there is about 100–200 \hbar OAM that remains in the mid-rapidity fluid at the beginning of hydrodynamic evolution. We further examine the effects of different hydrodynamic gradients on the spin polarizations of Λ and $\bar{\Lambda}$. The gradients of μ_B/T can change the ordering between Λ 's and $\bar{\Lambda}$'s polarizations.

DOI: [10.1103/PhysRevC.104.054908](https://doi.org/10.1103/PhysRevC.104.054908)

I. INTRODUCTION

Noncentral heavy-ion collisions carry angular momenta of the order of 10^3 – $10^4 \hbar$. After the initial impact, although most of the angular momentum is carried away by the spectator nucleons, a sizable fraction remains in the created quark-gluon plasma (QGP) and implies a nonzero rotational motion in the fluid. Such rotation inertia can lead to a strong vortical structure inside the resulting liquid. Local fluid vorticity can potentially induce a preferential orientation on the spins of the emitted particles through spin-orbit coupling. The STAR Collaboration at the BNL Relativistic Heavy-Ion Collider (RHIC) discovered the global polarization of Λ hyperons, which indicated fluid vorticity of $\omega \approx (9 \pm 1) \times 10^{21} \text{ s}^{-1}$ [1]. This result far surpasses the vorticity of all other known fluids in nature. The discovery of global hyperon polarization and three-dimensional (3D) simulations of the collision dynamics have opened an entirely new direction of research in heavy-ion physics. To understand the origin of the RHIC Λ polarization measurements, we need to address two key theoretical questions: (i) How do the global collision geometry and its orbital angular momentum (OAM) induce the local flow vorticity in heavy-ion collisions? (ii) How do fluid gradients act as thermodynamic forces to polarize the spins of particles? Resolving these two outstanding questions can provide crucial insights into emergent many-body phenomena in quantum chromodynamics (QCD).

Extensive theoretical and phenomenological investigations have been devoted to the effects of fluid vorticity on spin polarization [2–14] as well as the related transport phenomenon involving spin [15–24]. Hydrodynamics plus hadronic transport hybrid models and pure transport approaches can provide good descriptions of the global polarization for Λ and $\bar{\Lambda}$. However, the measured azimuthal distributions of polarization showed an opposite oscillation pattern compared to most of the theoretical results [25–29].

Most of the phenomenological studies assumed the Λ 's polarization is directly related to the local thermal vorticity. Recent works [30–35] proposed that the velocity shear tensor and gradients of μ_B/T can contribute to the spin polarization of Λ and $\bar{\Lambda}$. The effects of velocity shear tensor on the longitudinal polarization's azimuthal dependence were studied and found to be substantial [36–38]. These results suggest that the hyperon's polarization along the global orbital angular momentum direction is a cleaner observable to study the fluid vorticity evolution in heavy-ion collisions than the measurements of the longitudinal polarization.

This paper will focus on the global Λ polarization and study how the measurements can set constraints on the early-time longitudinal dynamics at the RHIC BES energies. In Sec. II, we will introduce a new parametric 3D initial condition model, generalized based on Ref. [39]. In particular, we introduce a model parameter to vary the early-time longitudinal distribution of fluid vorticity. We explicitly impose conservation of orbital angular momentum when mapping the initial collision geometry to hydrodynamic fields. Employing such a model enables us to quantitatively investigate how the global polarization measurements can set constraints on the early-time longitudinal dynamics in heavy-ion collisions.

*sangwook.ryu@wayne.edu

†ep9861@wayne.edu

‡chunshen@wayne.edu

The sensitivity of initial longitudinal flow in the pion's directed flow is studied with the same model. In Sec. III, our phenomenological study will show that a simultaneous description of Λ global polarization and the slope of the pion's directed flow set strong constraints on the initial condition parameter. The effects of different hydrodynamic gradients on Λ polarization will be quantified at the RHIC BES energies. We will conclude with some closing remarks in Sec. IV.

In this paper we use the conventions for the metric tensor $g^{\mu\nu} = \text{diag}(1, -1, -1, -1)$ and the Levi-Civita symbol $\epsilon^{0123} = 1$.

II. THE THEORETICAL FRAMEWORK

A. Initial-state orbital angular momentum (OAM) and mapping to hydrodynamic fields

The space-time structure of the initial collision dynamics can be modeled by the 3D Monte Carlo–Glauber model [39,40]. We can compute the system's total angular momentum based on the collision geometry before and after the collision impact. Individual nucleon i has its position and momentum $\{x_i^\mu, p_i^\mu\}$. We can compute the relativistic angular momentum as a bivector,

$$L_{\text{init}}^{\alpha\beta} \equiv x^\alpha p^\beta - x^\beta p^\alpha, \quad (1)$$

which has six independent components.

In fluid dynamics, we can define the angular momentum density tensor,

$$J^{\mu,\alpha\beta} = x^\alpha T^{\mu\beta} - x^\beta T^{\mu\alpha} + S^{\mu,\alpha\beta}. \quad (2)$$

Here the total angular momentum is composed by orbital and spin angular momentum tensors. We can write the orbital angular momentum tensor as

$$L^{\mu,\alpha\beta} = x^\alpha T^{\mu\beta} - x^\beta T^{\mu\alpha}. \quad (3)$$

According to [41], we can compute the system's angular momentum tensor on a hypersurface as

$$L_{\text{fluid}}^{\alpha\beta} = \int d^3\sigma_\mu L^{\mu,\alpha\beta}. \quad (4)$$

We choose the hypersurface along the constant longitudinal proper time $\tau = \sqrt{t^2 - z^2}$,

$$L_{\text{fluid}}^{\alpha\beta}(\tau) = \int \tau dx dy d\eta_s L^{\tau,\alpha\beta}. \quad (5)$$

In this work, we will exactly match the local energy and momentum from initial collision geometry to the hydrodynamic fields at hydrodynamic starting time $\tau = \tau_0$. This matching is done at each point on the transverse plane, so that it ensures the system's OAM is preserved from the initial state to the hydrodynamic phase,

$$L_{\text{init}}^{\alpha\beta} = L_{\text{fluid}}^{\alpha\beta}(\tau_0). \quad (6)$$

We generalize the geometric-based 3D initial conditions in Ref. [39]. Based on the Glauber geometry, the area density

of energy and longitudinal momentum at a given transverse position is given by

$$\begin{aligned} \frac{d}{d^2\mathbf{x}_T} E(x, y) &= [T_A(x, y) + T_B(x, y)] m_N \cosh(y_{\text{beam}}) \\ &\equiv M(x, y) \cosh(y_{\text{CM}}) \end{aligned} \quad (7)$$

$$\begin{aligned} \frac{d}{d^2\mathbf{x}_T} P_z(x, y) &= [T_A(x, y) - T_B(x, y)] m_N \sinh(y_{\text{beam}}) \\ &\equiv M(x, y) \sinh(y_{\text{CM}}). \end{aligned} \quad (8)$$

Here $T_{A(B)}(x, y)$ is the participant thickness function in the transverse plane, m_N is the mass of the nucleon, and $y_{\text{beam}} \equiv \text{arccosh}[\sqrt{s_{\text{NN}}}/(2m_N)]$ is the beam rapidity. We define the colliding nucleus A as the projectile with positive rapidity, while the nucleus B is the target flying toward the $-z$ direction. The invariant mass and center-of-mass rapidity can be expressed in terms of the participant thickness functions as follows:

$$M(x, y) = m_N \sqrt{T_A^2 + T_B^2 + 2T_A T_B \cosh(2y_{\text{beam}})}, \quad (9)$$

$$y_{\text{CM}}(x, y) = \text{arctanh}\left[\frac{T_A - T_B}{T_A + T_B} \tanh(y_{\text{beam}})\right]. \quad (10)$$

Requiring the energy and momentum to be conserved when mapping the initial condition to hydrodynamic fields, we get the following constraints on the system's energy-momentum tensor:

$$\begin{aligned} M(x, y) \cosh[y_{\text{CM}}(x, y)] &= \int \tau_0 d\eta_s [T^{\tau\tau}(x, y, \eta_s) \cosh(\eta_s) \\ &\quad + \tau_0 T^{\tau\eta}(x, y, \eta_s) \sinh(\eta_s)], \end{aligned} \quad (11)$$

$$\begin{aligned} M(x, y) \sinh[y_{\text{CM}}(x, y)] &= \int \tau_0 d\eta_s [T^{\tau\tau}(x, y, \eta_s) \sinh(\eta_s) \\ &\quad + \tau_0 T^{\tau\eta}(x, y, \eta_s) \cosh(\eta_s)]. \end{aligned} \quad (12)$$

Here $T^{\tau\tau}(x, y, \eta_s)$ and $T^{\tau\eta}(x, y, \eta_s)$ are components of the system's energy-momentum tensor on a constant proper time hypersurface with $\tau = \tau_0$. We assume the initial energy-momentum current has the following form:

$$T^{\tau\tau}(x, y, \eta_s) = e(x, y, \eta_s) \cosh(y_L), \quad (13)$$

$$T^{\tau\eta}(x, y, \eta_s) = \frac{1}{\tau_0} e(x, y, \eta_s) \sinh(y_L). \quad (14)$$

We ignore the transverse expansion and set transverse components $T^{\tau x} = T^{\tau y} = 0$ at $\tau = \tau_0$. Here we parametrize a nonzero longitudinal momentum with the rapidity variable

$$y_L \equiv f y_{\text{CM}}, \quad (15)$$

where $f \in [0, 1]$ is a parameter that controls the fraction of longitudinal momentum attributed to the flow velocity. When $f = 0$, $y_L = 0$, the conditions reduce to the well-known Bjorken flow scenario, which was used in Ref. [39]. This longitudinal momentum fraction parameter f allows us to vary the size of the initial longitudinal flow while keeping the net longitudinal momentum of the hydrodynamic fields fixed. Plugging Eqs. (13) and (14) into Eqs. (11) and (12),

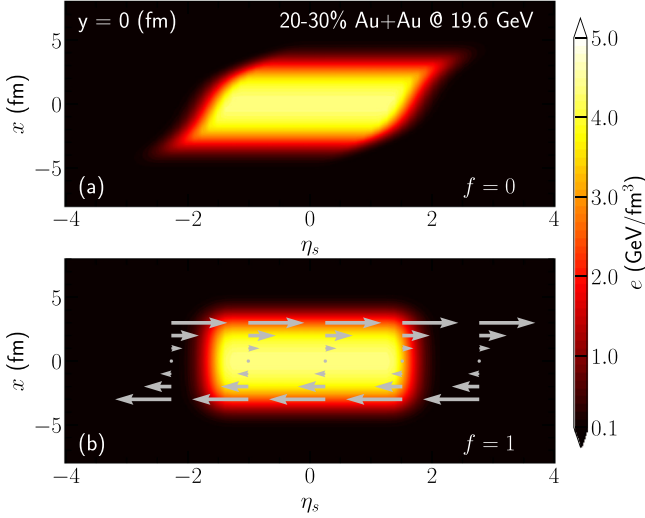


FIG. 1. Color contours show the initial energy density distributions in the x - η_s plane for 20–30% Au+Au collisions at 19.6 GeV with the longitudinal rapidity fractions $f = 0$ (a) and $f = 1$ (b). The grey arrows in panel (b) indicate the nonzero initial longitudinal flow u^η with $y_L = y_{CM}$ in Eqs. (13) and (14). $u^\eta = 0$ in panel (a).

we get

$$M(x, y) = \int \tau_0 d\eta_s e(x, y, \eta_s) \cosh(y_L + \eta_s - y_{CM}), \quad (16)$$

$$0 = \int \tau_0 d\eta_s e(x, y, \eta_s) \sinh(y_L + \eta_s - y_{CM}). \quad (17)$$

To satisfy these two equations, we can choose a symmetric rapidity profile parametrization with respect to $y_{CM} - y_L$ for the local energy density [42],

$$\begin{aligned} e(x, y, \eta_s; y_{CM} - y_L) \\ = \mathcal{N}_e(x, y) \exp \left[-\frac{(|\eta_s - (y_{CM} - y_L)| - \eta_0)^2}{2\sigma_\eta^2} \right] \\ \times \theta(|\eta_s - (y_{CM} - y_L)| - \eta_0). \end{aligned} \quad (18)$$

Here the parameter η_0 determines the width of the plateau and the σ_η controls how fast the energy density falls off at the edge of the plateau. In a highly asymmetric situation $T_A(x, y) \gg T_B(x, y)$, the center-of-mass rapidity $y_{CM}(x, y) \rightarrow y_{beam}$. To make sure there is not too much energy density deposited beyond the beam rapidity, we set $\eta_0 = \min[\eta_0, y_{beam} - (y_{CM} - y_L)]$. The normalization factor $\mathcal{N}_e(x, y)$ is not a free parameter in our model. It is determined by the local invariant mass $M(x, y)$,

$$\mathcal{N}_e(x, y) = \frac{M(x, y)}{2 \sinh(\eta_0) + \sqrt{\frac{\pi}{2}} \sigma_\eta e^{\sigma_\eta^2/2} C_\eta}, \quad (19)$$

$$C_\eta = e^{\eta_0} \operatorname{erfc} \left(-\sqrt{\frac{1}{2}} \sigma_\eta \right) + e^{-\eta_0} \operatorname{erfc} \left(\sqrt{\frac{1}{2}} \sigma_\eta \right). \quad (20)$$

Here $\operatorname{erfc}(x)$ is the complementary error function.

Figure 1 shows the two extreme scenarios for the energy density and flow distributions of our 3D initial condition for

20–30% Au+Au collisions at 19.6 GeV with the longitudinal rapidity fraction parameter $f = 0$ and $f = 1$. When $f = 0$, the local net longitudinal momentum leads to a shift of the energy density flux tube to the forward rapidity. With $f = 1$, the longitudinal momentum $P_z(x, y)$ is attributed to the longitudinal flow velocity instead. Let us note here that ensuring the net longitudinal momentum conservation introduces an anticorrelation between the shifts of the energy density flux tubes in the η_s direction and the size of the longitudinal flow velocity. As we will see in the following section, varying the parameter f results in strong dependencies in the Λ 's polarization and the slope of the pion's directed flow dv_1/dy . Therefore, these two experimental observables can tight constraints on the parameter f .

In addition to the initial energy and momentum distributions, the nonzero net baryon number current is considered for heavy-ion collisions in the RHIC BES program. The net-baryon number density current has the form of

$$J_B^\mu(x, y, \eta_s) = n_B(x, y, \eta_s) u^\mu(x, y, \eta_s). \quad (21)$$

Here $n_B(x, y, \eta_s)$ represents the local net baryon density:

$$n_B(x, y, \eta_s) = T_A(x, y) f_{n_B}^A(\eta_s) + T_B(x, y) f_{n_B}^B(\eta_s), \quad (22)$$

where its space-time rapidity dependence is characterized by asymmetric Gaussian functions $f_{n_B}^A$ and $f_{n_B}^B$ as in [43],

$$\begin{aligned} f_{n_B}^A(\eta_s) = \mathcal{N}_{n_B} \left\{ \theta(\eta_s - \eta_{B,0}) \exp \left[-\frac{(\eta_s - \eta_{B,0})^2}{2\sigma_{B,out}^2} \right] \right. \\ \left. + \theta(\eta_{B,0} - \eta_s) \exp \left[-\frac{(\eta_s - \eta_{B,0})^2}{2\sigma_{B,in}^2} \right] \right\}, \end{aligned} \quad (23)$$

$$\begin{aligned} f_{n_B}^B(\eta_s) = \mathcal{N}_{n_B} \left\{ \theta(\eta_s + \eta_{B,0}) \exp \left[-\frac{(\eta_s + \eta_{B,0})^2}{2\sigma_{B,in}^2} \right] \right. \\ \left. + \theta(-\eta_{B,0} - \eta_s) \exp \left[-\frac{(\eta_s + \eta_{B,0})^2}{2\sigma_{B,out}^2} \right] \right\}. \end{aligned} \quad (24)$$

The relevant parameters $\eta_{B,0}$, $\sigma_{B,in}$, and $\sigma_{B,out}$ are determined such that the net proton rapidity distribution is reproduced [39]. We will use the same initial-state model parameters as those in Table I of Ref. [39] and only vary the new longitudinal momentum fraction parameter f in this work. We have checked that the parameter f has negligible effects on most of the global observables such as the pseudorapidity distributions of particle yields, identified particles' mean p_T , and elliptic flow coefficient at mid-rapidity.

B. Hydrodynamic evolution and fluid vorticity

In this work, we use the open-source 3D viscous hydrodynamic code package MUSIC [43–47] to simulate fluid dynamical evolution of the system's energy, momentum, and net baryon density,

$$\partial_\mu T^{\mu\nu} = 0, \quad (25)$$

$$\partial_\mu J_B^\mu = 0, \quad (26)$$

where the energy-momentum tensor is defined as

$$T^{\mu\nu} = e u^\mu u^\nu - (P + \Pi) \Delta^{\mu\nu} + \pi^{\mu\nu}. \quad (27)$$

The system's energy-momentum tensor is composed of the local energy density e of the fluid cell, the thermal pressure P , the fluid velocity u^μ , and the shear stress tensor and bulk viscous pressure $\pi^{\mu\nu}$ and Π . The spatial projection tensor is defined as $\Delta^{\mu\nu} \equiv g^{\mu\nu} - u^\mu u^\nu$ with the metric $g^{\mu\nu} = \text{diag}(1, -1, -1, -1)$. Hydrodynamic equations are solved together with a lattice QCD based equation of state (EoS) at finite baryon density, NEOS-BQS, in which the strangeness neutrality condition and electric charge density $n_Q = 0.4n_B$ are imposed [48].

In this work, we do not consider viscous effects from bulk viscous pressure, $\Pi = 0$, nor the net baryon diffusion effects. The shear stress tensor is evolved according to the following equation of motion [49]:

$$\tau_\pi D\pi^{(\mu\nu)} + \pi^{\mu\nu} = 2\eta\sigma^{\mu\nu} - \delta_{\pi\pi}\pi^{\mu\nu}\theta + \varphi_7\pi_\alpha^{(\mu}\pi^{\nu)\alpha} - \tau_{\pi\pi}\pi_\alpha^{(\mu}\sigma^{\nu)\alpha} + \lambda_{\pi\Pi}\Pi\sigma^{\mu\nu}. \quad (28)$$

Here $D = u^\alpha \partial_\alpha$ is the comoving time derivative and $A^{(\mu\nu)} = \Delta_{\alpha\beta}^{\mu\nu} A^{\alpha\beta}$ denotes symmetrized and traceless projections with

$$\Delta_{\alpha\beta}^{\mu\nu} = \frac{1}{2}(\Delta^\mu_\alpha \Delta^\nu_\beta + \Delta^\nu_\alpha \Delta^\mu_\beta) - \frac{1}{3}\Delta^{\mu\nu} \Delta_{\alpha\beta}. \quad (29)$$

In Eq. (28), η denotes the shear viscosity and τ_π is the relaxation time, which controls the time scale for the shear stress tensor to relax to its Navier-Stokes value. The velocity shear tensor is defined as $\sigma^{\mu\nu} \equiv \frac{1}{2}(\nabla^\mu u^\nu + \nabla^\nu u^\mu) - \frac{1}{3}\Delta^{\mu\nu}(\nabla \cdot u)$, where $\nabla^\mu = \Delta^{\mu\alpha} \partial_\alpha$. Additional second-order gradient terms are included with their transport coefficients $\{\delta_{\pi\pi}, \phi_7, \tau_{\pi\pi}, \lambda_{\pi\Pi}\}$ according to the DNMR hydrodynamic theory [49,50]. We use a temperature and μ_B dependent specific shear viscosity $(\eta/s)(T, \mu_B)$ in our hydrodynamic simulations as in Ref. [39]. This $(\eta/s)(T, \mu_B)$ is constrained by the elliptic flow measurements from the RHIC BES phase I [51].

During hydrodynamic simulations, the fluid kinematic vorticity tensor can be computed as

$$\omega_K^{\mu\nu} \equiv \frac{1}{2}(\partial^\nu u^\mu - \partial^\mu u^\nu). \quad (30)$$

One can also define the transverse kinematic vorticity tensor with the spatial projection operator,

$$\omega_{K,\perp}^{\mu\nu} \equiv \frac{1}{2}(\nabla^\nu u^\mu - \nabla^\mu u^\nu), \quad (31)$$

The transverse kinematic vorticity differs from the kinematic vorticity tensor by the local acceleration,

$$\begin{aligned} \omega_{K,\perp}^{\mu\nu} &\equiv \frac{1}{2}(\partial^\nu u^\mu - \partial^\mu u^\nu) - \frac{1}{2}(u^\nu Du^\mu - u^\mu Du^\nu) \\ &= \omega_K^{\mu\nu} - \frac{1}{2}(u^\nu Du^\mu - u^\mu Du^\nu). \end{aligned} \quad (32)$$

The thermal vorticity is defined as

$$\begin{aligned} \omega_{\text{th}}^{\mu\nu} &\equiv \frac{1}{2}\left[\partial^\nu\left(\frac{u^\mu}{T}\right) - \partial^\mu\left(\frac{u^\nu}{T}\right)\right] \\ &= \frac{1}{T}\left\{\omega_K^{\mu\nu} - \frac{1}{2T}[(\partial^\nu T)u^\mu - (\partial^\mu T)u^\nu]\right\} \end{aligned} \quad (33)$$

and the T -vorticity is

$$\begin{aligned} \omega_T^{\mu\nu} &\equiv \frac{1}{2}[\partial^\nu(Tu^\mu) - \partial^\mu(Tu^\nu)] \\ &= T\left\{\omega_K^{\mu\nu} + \frac{1}{2T}[(\partial^\nu T)u^\mu - (\partial^\mu T)u^\nu]\right\}. \end{aligned} \quad (34)$$

The thermal and T -vorticity tensors receive opposite contributions from the temperature gradient terms. We will explore the theoretical uncertainty of computing the hyperon's spin polarization with different types of vorticity tensors in Appendix A.

C. Evolution of the fluid vorticity near mid-rapidity

We define the collision impact parameter along the $+x$ direction and it points from the target nucleus to the projectile. In this convention, the global OAM points in the $-y$ direction. The Λ hyperon's global polarization is defined as its polarization component along the global OAM direction, which is related to the xz component of the thermal vorticity tensor $\omega_{\text{th}}^{\mu\nu}$. It is instructive first to study the time evolution of ω_{th}^{xz} during the hydrodynamic evolution. We define the thermal vorticity averaged over a given space-time volume weighted by the local energy density,

$$\langle\omega_{\text{th}}^{\mu\nu}\rangle(\tau) = \frac{\int_{\eta_s^{\min}}^{\eta_s^{\max}} d\eta_s \int d^2x_\perp e \omega_{\text{th}}^{\mu\nu}}{\int_{\eta_s^{\min}}^{\eta_s^{\max}} d\eta_s \int d^2x_\perp e}. \quad (35)$$

For mid-rapidity fluid cells, we choose a symmetric space-time rapidity window, $\eta_s^{\min} = -0.5$ and $\eta_s^{\max} = 0.5$.

As Fig. 1 illustrated, the longitudinal rapidity fraction parameter f controls how much of the global OAM is attributed to the initial local fluid vorticity. We find that the initial averaged fluid vorticity $\langle\omega_{\text{th}}^{\mu\nu}\rangle$ has a good linear dependence on the model parameter f .

Figure 2(a) shows the evolution of the averaged fluid vorticity in 20–30% Au+Au collisions at 200 GeV with different values of f . With the parameter $f = 0$, all the system's OAM is attributed to the shifts of energy density flux tubes along the η_s direction. The entire system starts with zero fluid vorticity ω_{th}^{xz} at the beginning of hydrodynamic simulations. We observe that the averaged $\langle\omega_{\text{th}}^{xz}\rangle$ increases rapidly during the first fm/c of the hydrodynamic evolution and saturates around with a magnitude of 10^{-4} afterward. Our result suggests that the pressure gradients inside the fluid can develop vorticity within a timescale of 1 fm/c, but the size is small at 200 GeV. With a nonzero f value in the initial-state model, a fraction of the OAM is attributed to nonzero initial fluid vorticity. In these cases, the averaged $\langle\omega_{\text{th}}^{xz}\rangle$ decreases monotonically as a function of τ . This qualitatively different time evolution between $f = 0$ and $f \neq 0$ indicates that the initial-state longitudinal flow distribution dominates the fluid thermal vorticity ω_{th}^{xz} (related to the global polarization) in heavy-ion collisions.

Figure 2(b) shows the evolution of the averaged fluid vorticity $\langle\omega_{\text{th}}^{xz}\rangle(\tau)$ in four centrality bins in Au+Au collisions at 200 GeV. With all the model parameter fixed, the initial fluid vorticity is larger in the more peripheral centrality bin. This centrality dependence is because of the large local asymmetry between T_A and T_B in the peripheral collisions. The time

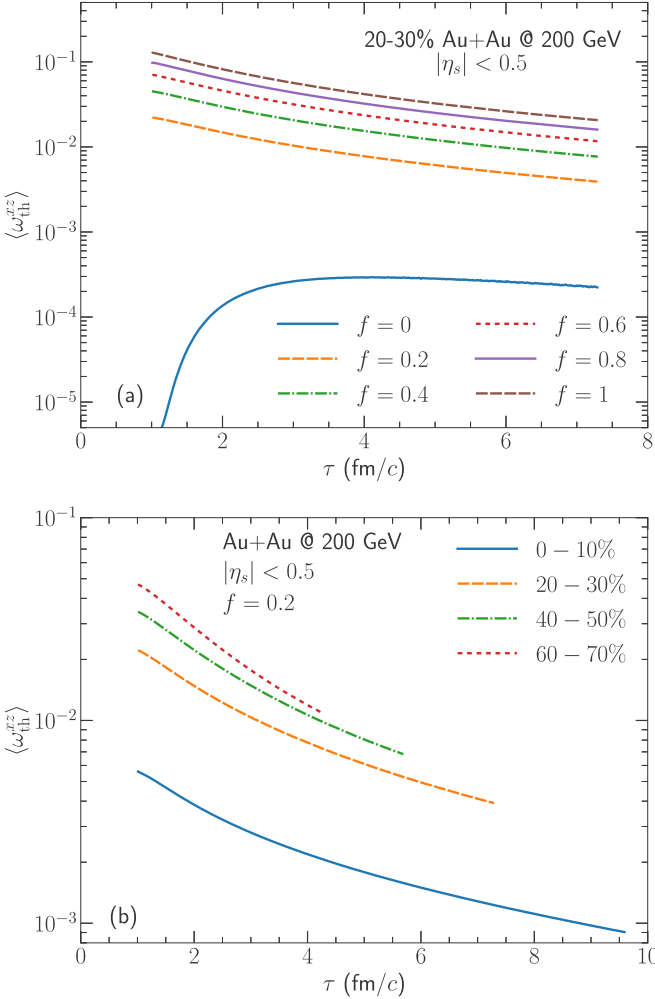


FIG. 2. (a) Time evolution of the averaged thermal vorticity of fluid with different longitudinal rapidity fraction f in mid-rapidity 20–30% Au+Au collisions at 200 GeV. (b) Time evolution of the averaged thermal vorticity of fluid for four centrality bins in Au+Au collisions at 200 GeV with $f = 0.2$.

evolution of $\langle \omega_{th}^{xz} \rangle(\tau)$ is qualitatively the same for all centrality bins in the hydrodynamic phase. Our results have qualitatively the same behavior as those in the transport models [15].

D. The averaged spin vector of fermions

For spin-1/2 fermions, the average spin vector (defined as the Pauli-Lubanski vector) over the hypersurface Σ_μ can be computed as [34]

$$S^\mu(p^\mu) = \frac{1}{4m} \int d^3 \Sigma_\alpha p^\alpha \mathcal{A}^\mu. \quad (36)$$

Here, the axial vector is defined as

$$\mathcal{A}^\mu = \beta n_0(E)[1 - n_0(E)] \epsilon^{\mu\nu\alpha\gamma} \left[-\frac{1}{2\beta} p_\nu \omega_{\alpha\gamma}^{\text{th}} - \frac{b_i}{\beta E} u_\nu p_{\perp\alpha} \nabla_\gamma \frac{\mu_B}{T} - \frac{p_\perp^2}{E} u_\nu Q_\alpha{}^\rho \sigma_{\rho\gamma} \right], \quad (37)$$

where $E = p^\mu u_\mu$, $p_\perp^\mu = \Delta^{\mu\nu} p_\nu$, and $Q^{\mu\nu} = -\frac{p_\perp^\mu p_\perp^\nu}{p_\perp^2} + \frac{1}{3} \Delta^{\mu\nu}$. Here $\epsilon^{\mu\rho\sigma\tau}$ is the Levi-Civita tensor and we choose the convention $\epsilon^{txyz} = 1$. We denote the term related to $\nabla_\gamma(\mu_B/T)$ as the μ_B -induced polarization (μ_B IP) [33] and the last term related to the velocity shear tensor as the shear-induced polarization (SIP)¹ [34,35]. Equations (36) and (37) assume that the hypersurface fluid cells reach local thermal equilibrium. The fermions emitted at early time of the evolution could receive sizable out-of-equilibrium corrections.

In this work, we compute Λ 's and $\bar{\Lambda}$'s spins on a constant energy hypersurface with $e = e_{\text{sw}}$, on which fluid cells are converted to hadrons via the Cooper-Frye prescription. Hadrons are further fed to the URQMD hadronic transport. Because URQMD does not distinguish hadrons' spins in their evolution, we assume the spins of Λ and $\bar{\Lambda}$ are frozen out at $e = e_{\text{sw}}$ in this work. The values of e_{sw} are adjusted to match the proton yield in every collision energy at the RHIC BES program [52]. We will study how our results depend on the choice of e_{sw} in Appendix B.

The averaged polarization vector in the laboratory frame is

$$P_{\text{lab}}^\mu(p^\mu) = S^\mu(p^\mu)/\langle S \rangle. \quad (38)$$

In the RHIC experiments, the polarizations of Λ and $\bar{\Lambda}$ are measured in the particle's local rest frame,

$$P^t(p^\mu) = \frac{p^0}{m} P_{\text{lab}}^t(p^\mu) - \frac{\vec{p} \cdot \vec{P}_{\text{lab}}(p^\mu)}{m} = 0 \quad (39)$$

and

$$P^i(p^\mu) = P_{\text{lab}}^i(p^\mu) - \frac{\vec{p} \cdot \vec{P}_{\text{lab}}(p^\mu)}{p^0(p^0 + m)} p^i. \quad (40)$$

In the Λ 's local rest frame, the time component of P^μ is zero, which serves as a nontrivial test for the numerical implementations.

It is instructive to understand the time development of the Λ hyperon's polarization during hydrodynamic evolution. Based on Eqs. (36) and (38), we can compute the differential polarization vector as a function of the hydrodynamic proper time τ ,

$$P_{\text{lab}}^\mu(p^\mu, \tau) = \lim_{\Delta\tau \rightarrow 0} \frac{1}{\langle S \rangle} \frac{1}{4m} \frac{\int_\tau^{\tau+\Delta\tau} d^3 \Sigma_\alpha p^\alpha \mathcal{A}^\mu}{\int_\tau^{\tau+\Delta\tau} d^3 \Sigma_\alpha p^\alpha n_0(E)}. \quad (41)$$

We then boost the $P_{\text{lab}}^\mu(p^\mu, \tau)$ to the hyperon's local rest frame with Eq. (40) and denote it as $P^\mu(p^\mu, \tau)$. Please note that we normalize the differential polarization vector by the number of hyperons emitted within the $\Delta\tau$ interval,

$$\frac{dN}{d\tau}(p^\mu, \tau) = \lim_{\Delta\tau \rightarrow 0} \frac{1}{\Delta\tau} \int_\tau^{\tau+\Delta\tau} d^3 \Sigma_\alpha p^\alpha n_0(E). \quad (42)$$

¹We notice that the shear-induced polarization term has a different expression in [35], where u_ν was replaced by a global time vector $t_\nu = (1, 0, 0, 0)$ and the $\sigma_{\rho\gamma}$ included additional temperature gradients. While the exact form of the SIP is still under debate, we will carry out calculations with the SIP definition in Eq. (37) in this work. Our conclusions do not depend on the exact forms of the SIP term.

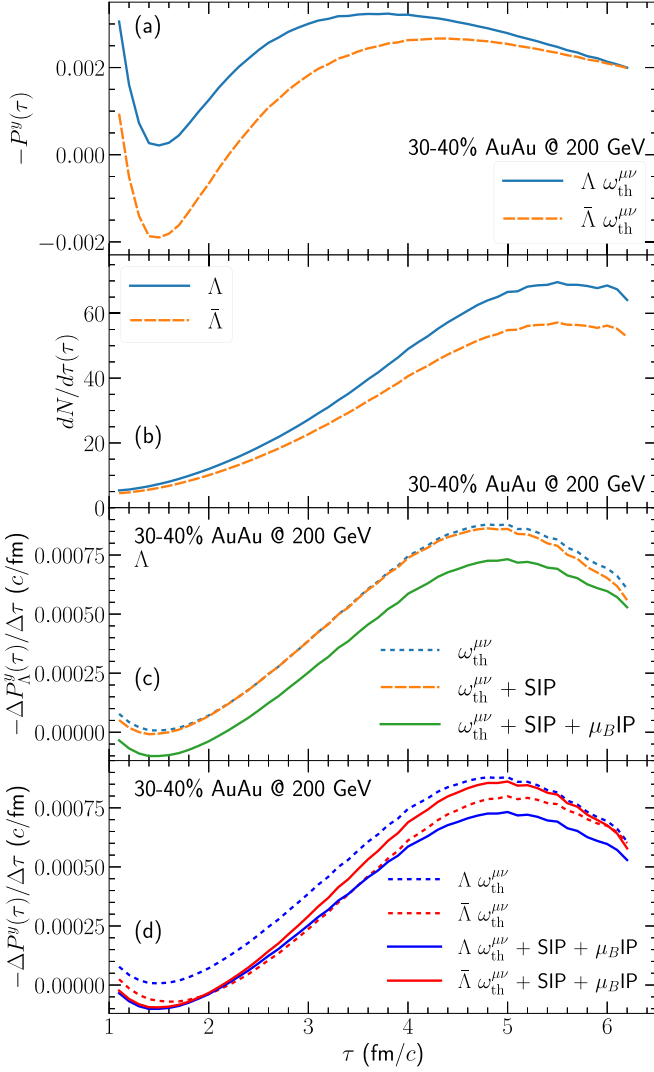


FIG. 3. (a) The hyperon's global polarization as a function of hydrodynamic proper time. (b) The hyperon production as a function of τ . (c) The time development of Λ 's global polarization with different fluid gradients. (d) The comparison of Λ 's and $\bar{\Lambda}$'s global polarization developments. The results are for Λ and $\bar{\Lambda}$ with $p_T \in [0.5, 3.0]$ GeV and $|y| < 1$ in 30–40% Au+Au collisions at 200 GeV with the longitudinal rapidity fraction $f = 0.2$.

The momentum-integrated hyperon polarization at time τ can be computed as a yield-weighted average,

$$P^\mu(\tau) = \frac{\int \frac{d^3p}{E} P^\mu(p^\mu, \tau) \frac{dN}{d\tau}(p^\mu, \tau)}{\int \frac{d^3p}{E} \frac{dN}{d\tau}(p^\mu, \tau)}. \quad (43)$$

To study $P^\mu(\tau)$'s contribution to the total hyperon polarization, we need to weight $P^\mu(\tau)$ with the number of hyperon emitted at every time step τ ,

$$\frac{\Delta P^\mu}{\Delta\tau}(\tau) = \frac{P^\mu(\tau) \int \frac{d^3p}{E} \frac{dN}{d\tau}(p^\mu, \tau)}{\int d\tau \int \frac{d^3p}{E} \frac{dN}{d\tau}(p^\mu, \tau)}. \quad (44)$$

Figure 3(a) shows that the averaged hyperon polarization as a function of the longitudinal proper time. The $P^y(\tau)$ drops

sharply during the first 0.5 fm/c, following the evolution of averaged $\langle\omega_{th}^{xz}\rangle$ in Fig. 2. Then $P^y(\tau)$ gradually increases and reaches its peak around 2.5 fm/c in the hydrodynamic evolution, which is from the ω_{th}^{xz} 's contribution in Eq. (37). Figure 3(b) shows that the hyperon production is dominated by the timelike surface elements (enhanced by the τ factor in the Jacobian) in the Cooper-Frye particlization at late time. By weighting $P^y(\tau)$ with the number of hyperons emitted at every time step in Eq. (44), we find that most contributions to the total polarization come from late time of the hydrodynamic evolution, as shown in Figs. 3(c) and 3(d). Although the early-time emitted hyperons are also largely polarized and could receive sizable out-of-equilibrium corrections, their net contributions to the total polarization remain small. Figure 3(c) demonstrates the effects of different fluid gradients in Eq. (37) on the development of Λ 's global polarization during hydrodynamic evolution. The thermal vorticity gives the dominant contribution to Λ 's global polarization. The contribution of shear-induced polarization (SIP) to the integrated global polarization is negligible, as expected from its tensor structure in Eq. (37). The μ_B/T gradients suppress the Λ 's global polarization by roughly a constant over time.

Figure 3(d) further compares the time developments of Λ 's and $\bar{\Lambda}$'s global polarization in 30–40% Au+Au collisions at 200 GeV. With the nonzero baryon density in the fluid, Λ hyperons receive larger contributions to their global polarization from the fluid thermal vorticity than those to $\bar{\Lambda}$. This effect is caused by the μ_B 's dipolar transverse distribution in the forward and backward space-time rapidities, which imprint the shapes of the projectile and target nuclei's nuclear thickness functions as in Eq. (22). The μ_B -gradient-induced polarization (μ_{BIP}) gives opposite contributions to Λ and $\bar{\Lambda}$. It cancels the difference between Λ and $\bar{\Lambda}$ during the first two fm/c of the evolution and contributes more to $\bar{\Lambda}$ in the late stage.

III. POLARIZATION RESULTS AT THE RHIC BES PROGRAM

Before we compare our calculations of the Λ 's and $\bar{\Lambda}$'s global polarization with the RHIC BES measurements, it is essential to understand the effects of the longitudinal rapidity fraction parameter f on various experimental observables. On the one hand, we checked that this model parameter does not have noticeable effects on particle rapidity distribution, mean transverse momentum, or elliptic flow coefficient at mid-rapidity. On the other hand, it shows strong sensitivity to the Λ 's global polarization and the slope of rapidity dependent π 's directed flow, $dv_1/dy|_{y=0}$. These two experimental observables are sensitive probes of the initial longitudinal flow and the energy density's space-time rapidity distribution.

Figure 4 shows that the magnitudes of Λ 's global polarization are very sensitive to the value of the longitudinal rapidity fraction parameter f in our model. With $f = 0$, the entire fluid starts with zero ω^{xz} at the beginning of hydrodynamics. The P_Λ^y remains almost zero in the mid-rapidity region, which is expected from the thermal vorticity evolution shown in Fig. 2. We find that a constant $f = 0.15$ can give a good description of the centrality dependence of the P_Λ^y in Au+Au collisions at 200 GeV, while the results with $f = 0.5$ already

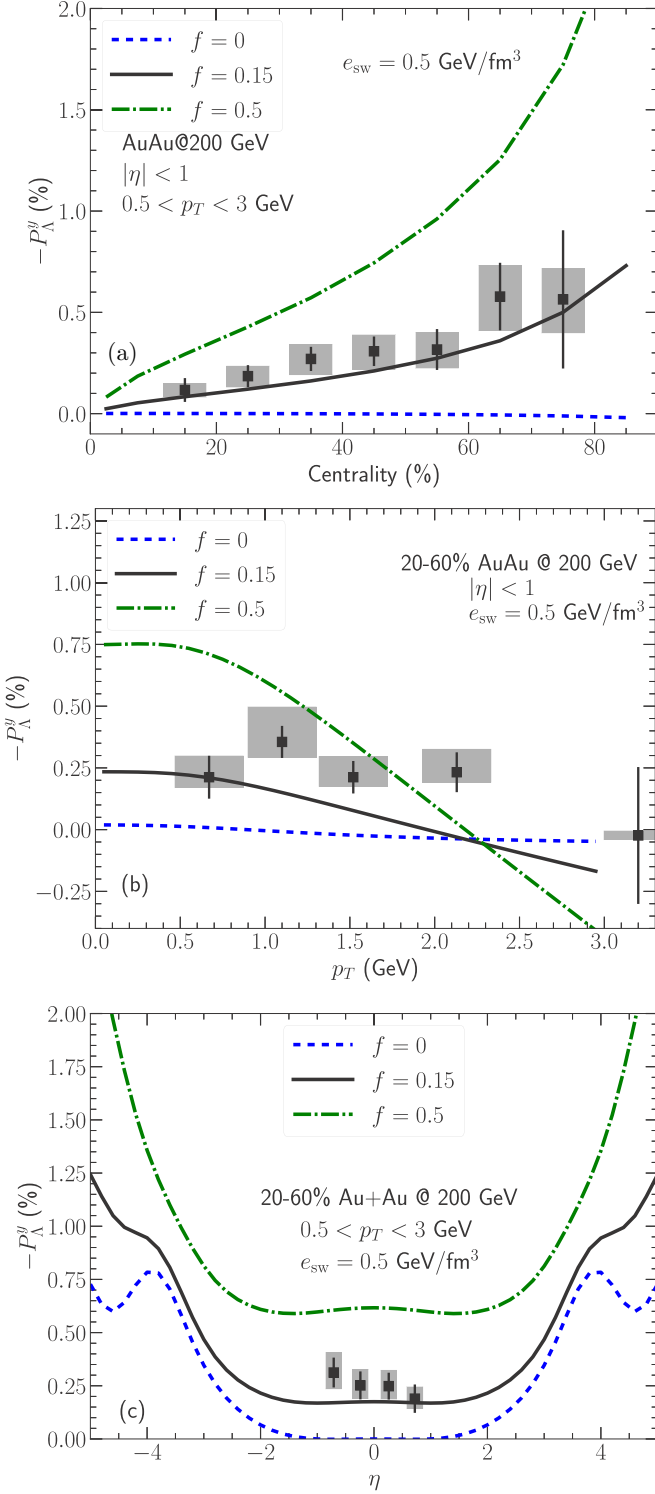


FIG. 4. The global Λ polarization's dependence on the initial-state longitudinal rapidity fraction in Au+Au collisions at 200 GeV compared with the STAR measurements [53]. The Λ 's global polarization is computed with all the gradient terms in Eq. (37). Panel (a) shows the P_{Λ}^y 's centrality dependence. Panel (b) presents the p_T differential P_{Λ}^y in 20–60% Au+Au collisions. Panel (c) shows the pseudorapidity dependence of P_{Λ}^y .

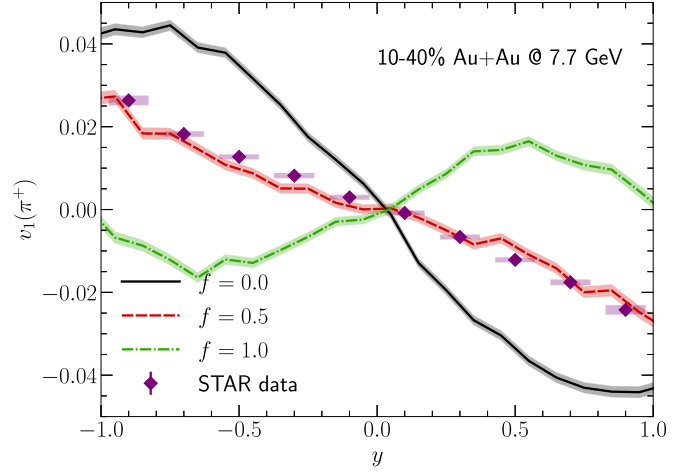


FIG. 5. The directed flow of π^+ as a function of rapidity with different initial-state longitudinal rapidity fraction f for 10–40% Au+Au collisions at 7.7 GeV compared with the STAR measurement [54].

overestimate the STAR measurements by a factor of 2. Figure 4(b) shows that the global polarization decreases monotonically as a function of p_T . Due to the presence of the thermal distribution $n_0(p \cdot u)$ in the expression for the polarization, one can also anticipate that the global spin polarization can receive significant contribution from \mathcal{A}^μ at low momentum. At zero transverse momentum limit $p^\mu = (m, 0, 0, 0)$,

$$P^y = P_{\text{lab}}^y \propto \mathcal{A}^y = n_0(m)(1 - n_0(m)) \left[-m\omega_{\text{th}}^{xz} - b_i \left(-u^x \partial^z \frac{\mu_B}{T} + u^z \partial^x \frac{\mu_B}{T} \right) + \frac{m}{T} (-u^x \sigma^{tz} + u^z \sigma^{tx}) \right]. \quad (45)$$

We have checked that the dominant numerical contribution comes from the thermal vorticity tensor ω_{th}^{xz} . Therefore, the global polarization at zero transverse momentum is directly related to the fluid thermal vorticity component ω_{th}^{xz} , recovering the nonrelativistic limit. For finite p_T , the ω_{th}^{tx} and ω_{th}^{tz} give additional relativistic contributions to Λ 's polarization. A larger longitudinal rapidity fraction f in the initial condition results in a larger global polarization P^y at $p_T = 0$ and a steeper decrease as p_T increases.

Finally, Fig. 4(c) shows the pseudorapidity dependence of P_{Λ}^y . In semiperipheral Au+Au collisions at 200 GeV, the polarization P_{Λ}^y has a plateau for $|\eta| < 2$ and increases in the forward and backward rapidity regions. Different values of f shift the magnitude of $P^y(\eta)$ by constants for $|\eta| < 2$.

Figure 5 shows a strong positive correlation between the slope of the pion's directed flow and the initial longitudinal rapidity fraction parameter f in our model. As the value of f varies from 0 to 1 in the model, there are fewer longitudinal

shifts of initial energy density distribution, as shown in Fig. 1, which result in a reduction of dipolar transverse deformation in the initial energy density profile in forward and backward space-time rapidities. Therefore, simulations with a large f value give a small slope for the pion's directed flow dv_1/dy at mid-rapidity. We find that $f = 0.5$ is preferred for Au+Au collisions at 7.7 GeV compared with the STAR measurements.

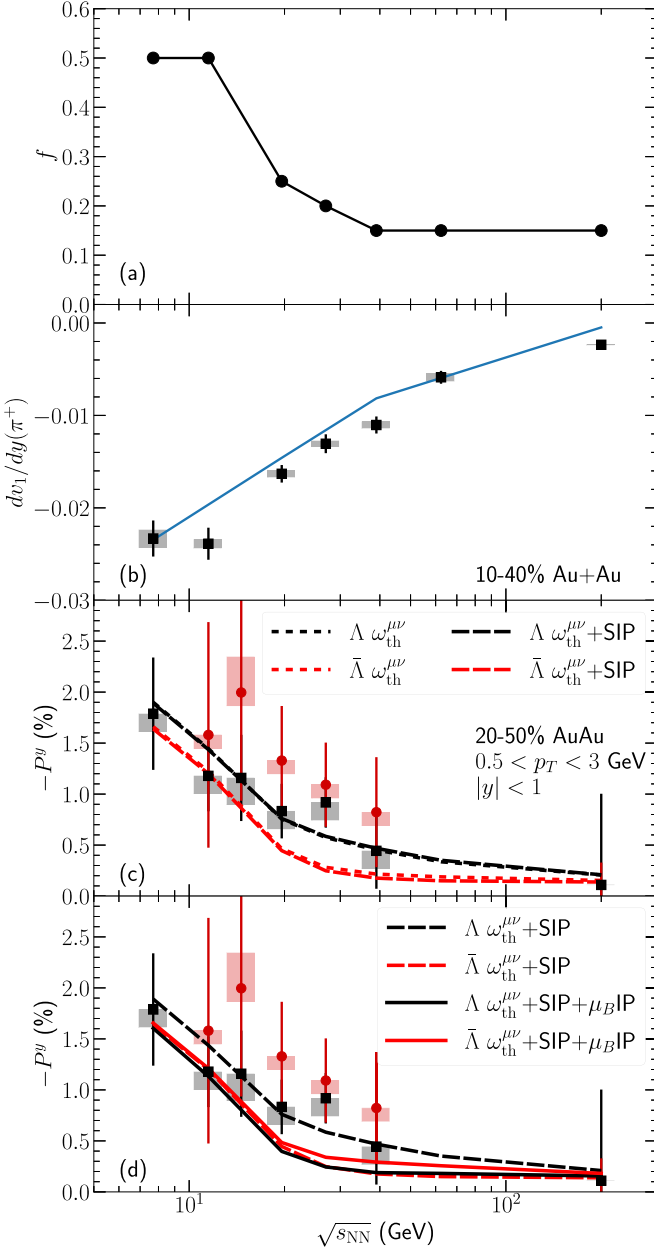


FIG. 6. (a) The value of longitudinal rapidity fraction f as a function of collision energy. (b) The slope of π^+ directed flow at $y = 0$, $dv_1/dy|_{y=0}$, compared with the STAR measurements [54]. (c),(d) The global Λ polarization in 20–50% Au+Au collisions as a function of collision energy. Calculations including different gradient terms are compared with the STAR measurements [1]. The STAR polarization data points are rescaled by 0.877 because of the latest hyperon decay parameter α_Λ [55].

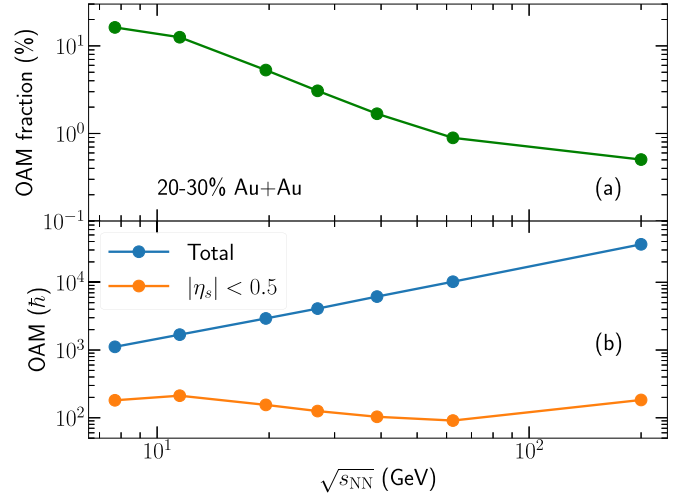


FIG. 7. (a) The percentage fraction of orbital angular momentum (OAM) in the mid-rapidity region $|\eta_s| < 0.5$ relative to the system's total OAM from the participant nucleons for 20–30% Au+Au collisions at the RHIC BES energies. (b) The system's total and mid-rapidity OAM as a function of the collision energy.

The positive dv_1/dy in the $f = 1$ case is generated by the dipolar deformation of the initial state net baryon density in the calculation.

Figures 4 and 5 show that the longitudinal rapidity fraction parameter f can be tightly constrained by these two experimental observables. Figure 6 shows the main results of this work. We adjust the parameter f at every collision energy to match the slope of the pion's directed flow at mid-rapidity and make predictions for Λ 's global polarization. We find that the f increases from 0.15 to 0.5 as the collision energy goes down from 200 to 7.7 GeV. A larger f is needed at lower collision energy, indicating that more longitudinal momentum of the system is attributed to the initial longitudinal flow velocity at the lower collision energy. The initial density and velocity profiles for hydrodynamics are further away from the Bjorken boost-invariant assumption at the lower collision energy. With the parameter f constrained by the pion's directed flow measurements, our model shows a reasonable description of the global polarization of Λ and $\bar{\Lambda}$ in Fig. 6(c).

With the constrained f in our model, we can estimate the amount of OAM left in the fluid at mid-rapidity after the initial impact at different collision energies. Based on OAM given by Eq. (4), Fig. 7 shows that only about 0.5% of the total OAM remains in the mid-rapidity region of 20–30% Au+Au collisions at 200 GeV. This relative fraction of OAM increases as the collision energy goes down. At 7.7 GeV, the relative fraction increases up to $\approx 15\%$ of the total OAM in the collision systems. Figure 7(b) shows that although the total OAM increases with collision energy the absolute OAM in the mid-rapidity region remains around 100–200 \hbar for 20–30% Au+Au collisions from 7.7 to 200 GeV.

We make further comparisons with different gradient terms in the global polarization observables in Figs. 6(c) and 6(d). We note that thermal vorticity gives the dominant contribution to the global Λ polarization. The shear-induced polarization is negligible, while the μ_B -induced polarization flips the

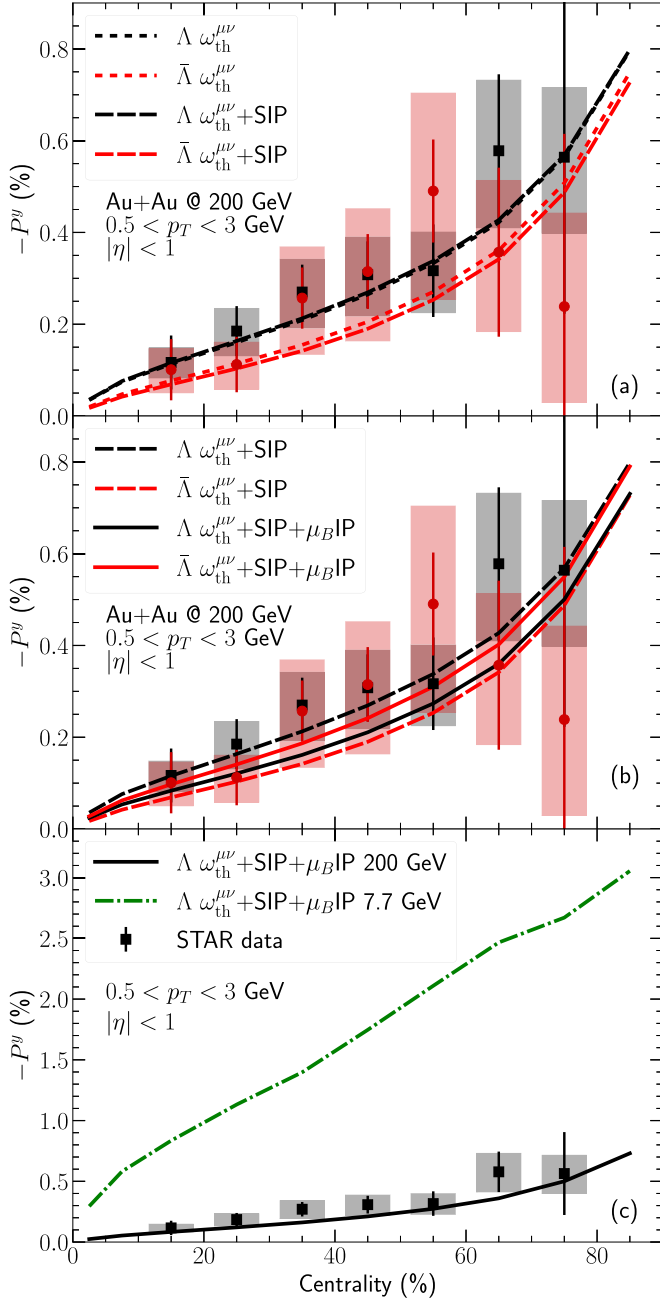


FIG. 8. (a),(b) The centrality dependence of the global Λ polarization with different gradient terms in Au+Au collisions at 200 GeV compared with the STAR measurements [53]. (c) Model prediction for P^y_{Λ} at 7.7 GeV. The STAR polarization data points are rescaled by 0.877 because of the latest hyperon decay parameter α_{Λ} [55].

ordering between Λ 's and $\bar{\Lambda}$'s polarizations at all energies. This result demonstrates that the μ_B distribution inside fluid is important to determine the difference between the Λ 's and $\bar{\Lambda}$'s polarizations. This conclusion is inline with the finding in Ref. [56].

In Figs. 8, 9, and 10, we further compare the centrality, p_T , and pseudorapidity dependence of Λ 's and $\bar{\Lambda}$'s global polar-

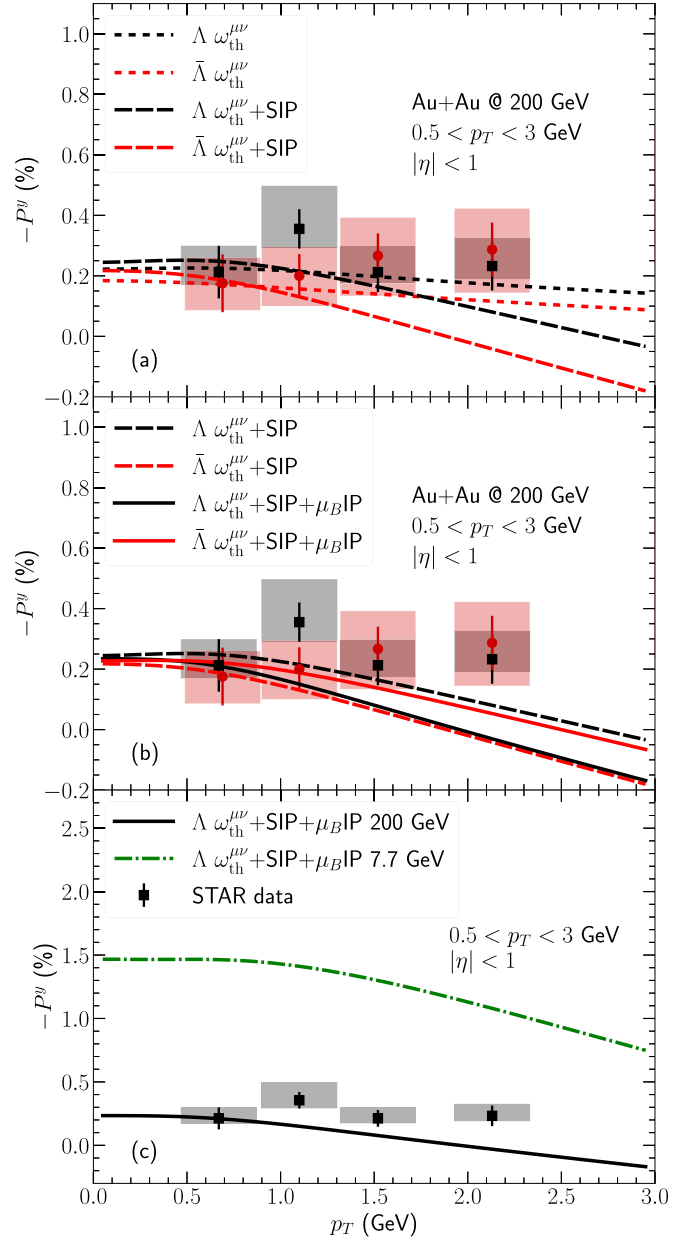


FIG. 9. (a),(b) The p_T -differential polarization for Λ with different gradient terms in 20–60% Au+Au collisions compared with the STAR measurements [53]. (c) Model prediction for $P^y_{\Lambda}(p_T)$ at 7.7 GeV. The STAR polarization data points are rescaled by 0.877 because of the latest hyperon decay parameter α_{Λ} [55].

ization with the STAR measurements at 200 GeV, respectively [53].

Figures 8(a) and 8(b) show that our model calculations provide a good description of the centrality dependence of the STAR data at 200 GeV. The μ_B IP terms reverse the difference between Λ 's and $\bar{\Lambda}$'s global polarizations, which suggests that the evolution net baryon density and its gradients are crucial to understand the difference between Λ 's and $\bar{\Lambda}$'s global polarizations. Figure 8(c) further show our prediction for the Λ polarization at 7.7 GeV with all the gradient terms included.

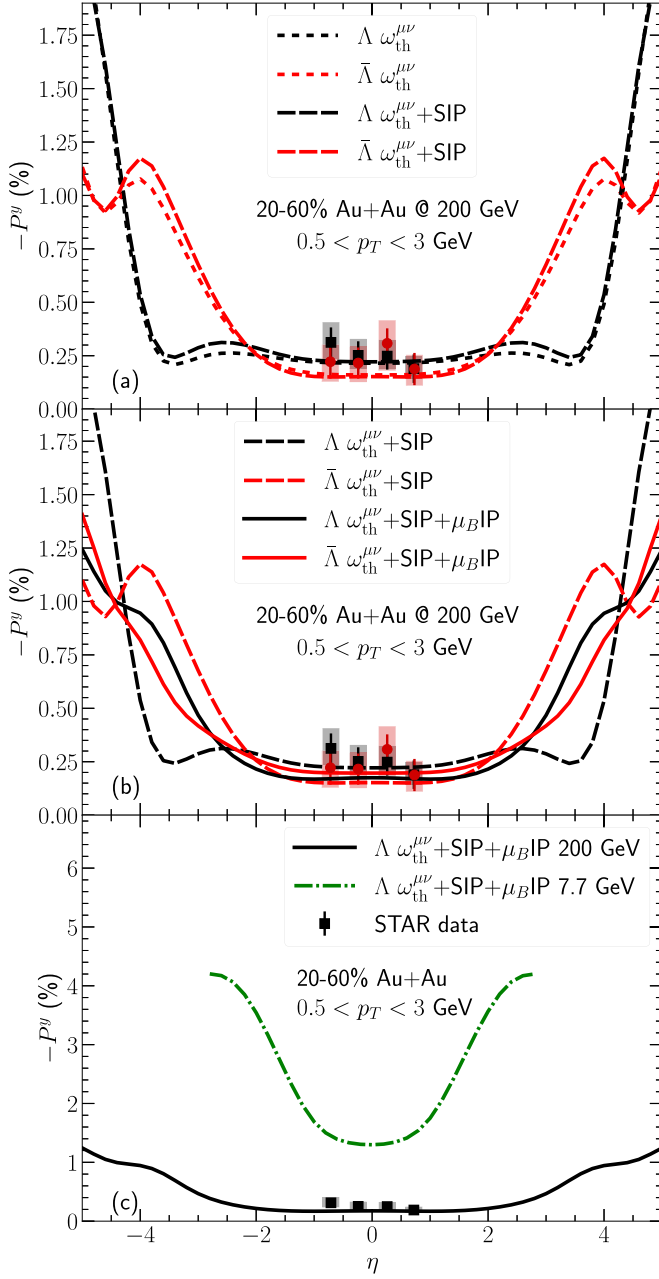


FIG. 10. (a),(b) The pseudorapidity dependence of the Λ polarization with different gradient terms in 20–60% Au+Au collisions at 200 GeV compared with the STAR measurements [53]. (c) Model prediction for $P_\Lambda^y(\eta)$ at 7.7 GeV. The STAR polarization data points are rescaled by 0.877 because of the latest hyperon decay parameter α_Λ [55].

In Figs. 9(a) and 9(b), we find that our results with only thermal vorticity have a weak p_T dependence. According to Eq. (37), the SIP terms introduce a linear dependence of P^y on the hyperon’s momentum. Because the total contribution from the SIP terms vanishes when integrating over the momentum, they enhance the P^y in small p_T but suppress it for

$p_T > 1$ GeV. Despite the significant uncertainties contained in the current STAR measurements, our results with SIP show a stronger p_T dependence than the data. In the meantime, the μ_B IP terms invert the ordering between Λ and $\bar{\Lambda}$. Figure 9(c) shows our prediction at 7.7 GeV which has the same p_T dependence as those at 200 GeV.

Figures 10(a) and 10(b) show the pseudorapidity distribution of the global polarization for Λ and $\bar{\Lambda}$ at 200 GeV with different gradient terms. Both P_Λ^y and $P_{\bar{\Lambda}}^y$ have a plateau structure within $|\eta| < 2$. Using thermal vorticity results in a slightly larger polarization for Λ than that of $\bar{\Lambda}$. In the forward and backward rapidity regions $|\eta| > 2$, the magnitudes of P^y increase rapidly in our model. The μ_B IP terms give different contributions to Λ and $\bar{\Lambda}$ and reduce the difference in the forward and backward rapidity regions.

We further provide our model prediction with all the gradient terms included for 7.7 GeV in Fig. 10(c). The plateau window of Λ ’s polarization shrinks as the collision energy goes down. At 7.7 GeV, the P_Λ^y remains approximately constant within $|\eta| < 1$ and increases in the forward and backward rapidity regions.

IV. CONCLUSIONS

In this work, we develop a hybrid dynamical framework, which explicitly conserves energy, momentum, and orbital angular momentum from the initial collision geometry to the following hydrodynamic evolution. We introduce the longitudinal rapidity fraction parameter f to vary how local net longitudinal momentum is distributed to flow velocity and energy density rapidity profile. This model parameter controls the amount of fluid vorticity correlated with the initial OAM at the beginning of the hydrodynamics. We study the evolution of the fluid vorticity during the hydrodynamic phase and find that the fluid expansion monotonically reduces the space-time averaged fluid vorticity as a function of time. Therefore, the initial distribution of fluid vorticity has a strong correlation with vorticity values at particlization and the magnitude of the hyperon’s global spin polarization.

Our phenomenological studies have shown that the pion’s directed flow and global polarization of Λ hyperons together can set strong constraints on the size of initial longitudinal flow velocity at different collision energies. By fitting the STAR measurements, we quantify the amount of orbital angular momentum left in the mid-rapidity fluid after the initial impact. We find that about 0.5% of the total OAM remains at mid-rapidity for 20–30% Au+Au collisions at 200 GeV, and this relative fraction increases to $\approx 15\%$ at 7.7 GeV. The centrality, p_T , and pseudorapidity dependence of P_Λ^y show reasonable agreement with the STAR measurements at 200 GeV.

We further quantify the effects of new gradient terms proposed in Refs. [32–35] on the global spin polarization of Λ hyperons. The global polarization P_Λ^y receives the dominant contribution from the fluid’s thermal vorticity at the particlization hypersurface. The shear-induced polarization introduces a sizable p_T dependence to Λ ’s global polarization, while its net effect on the integrated polarization is small. The

μ_B -induced polarization can alter the ordering between Λ 's and $\bar{\Lambda}$'s global polarizations, which indicates that the difference between Λ 's and $\bar{\Lambda}$'s global polarizations may not be related to a nonzero magnetic field at freeze-out. A similar conclusion is made in Ref. [56].

ACKNOWLEDGMENTS

We thank Sean Gavin, Cheming Ko, Michael Lisa, George Moschelli, Jun Takahashi, Giorgio Torrieri, Sergei Voloshin, and Yi Yin for fruitful discussion. This work is supported in part by the U.S. Department of Energy (DOE) under Grant No. DE-SC0013460 and in part by the National Science Foundation (NSF) under Grant No. PHY-2012922. This research used resources of the National Energy Research Scientific Computing Center, which is supported by the Office of Science of the U.S. Department of Energy under Contract No. DE-AC02-05CH11231, with resources provided by the Open Science Grid, which is supported by the National Science Foundation and the U.S. Department of Energy's Office of Science, and resources of the high performance computing services at Wayne State University. This work also is supported by the U.S. Department of Energy, Office of Science, Office of Nuclear Physics, within the framework of the Beam Energy Scan Theory (BEST) Topical Collaboration.

APPENDIX A: ESTIMATE SPIN POLARIZATION WITH DIFFERENT VORTICITY TENSORS

Within fluid dynamical evolution, different types of vorticity tensors can be defined, such as those in Eqs. (30)–(34). The authors in [28] proposed that calculating Λ spin polarization with the T -vorticity could reproduce the correct azimuthal dependence of the longitudinal polarization measured by the STAR Collaboration [57]. It is possible that the hyperon's spin polarization could be related to these fluid vorticity tensors. In this Appendix, we will compute the Λ 's global polarization with the vorticity tensors defined Eqs. (30)–(34),

$$S^\mu(p^\mu) = -\frac{1}{8m} \frac{\int d^3\Sigma_\alpha p^\alpha n_0(E)(1 - n_0(E))\epsilon^{\mu\nu\alpha\gamma} p_\nu \Omega_{\alpha\gamma}}{\int d^3\Sigma_\alpha p^\alpha n_0(E)}, \quad (\text{A1})$$

where $\Omega^{\alpha\gamma} = \frac{\omega_K^{\alpha\gamma}}{T}, \frac{\omega_{K,\perp}^{\alpha\gamma}}{T}, \omega_{\text{th}}^{\alpha\gamma}, \frac{\omega_T^{\alpha\gamma}}{T^2}$ [28]. We interpret their relative variations as the theoretical uncertainties in our calculations. The SIP's and μ_B IP's contributions remains the same as those shown in Figs. 8–10.

Figure 11 shows the centrality, p_T , and pseudorapidity dependence of global Λ polarization computed with different types of vorticity tensor. The kinematic, thermal, and

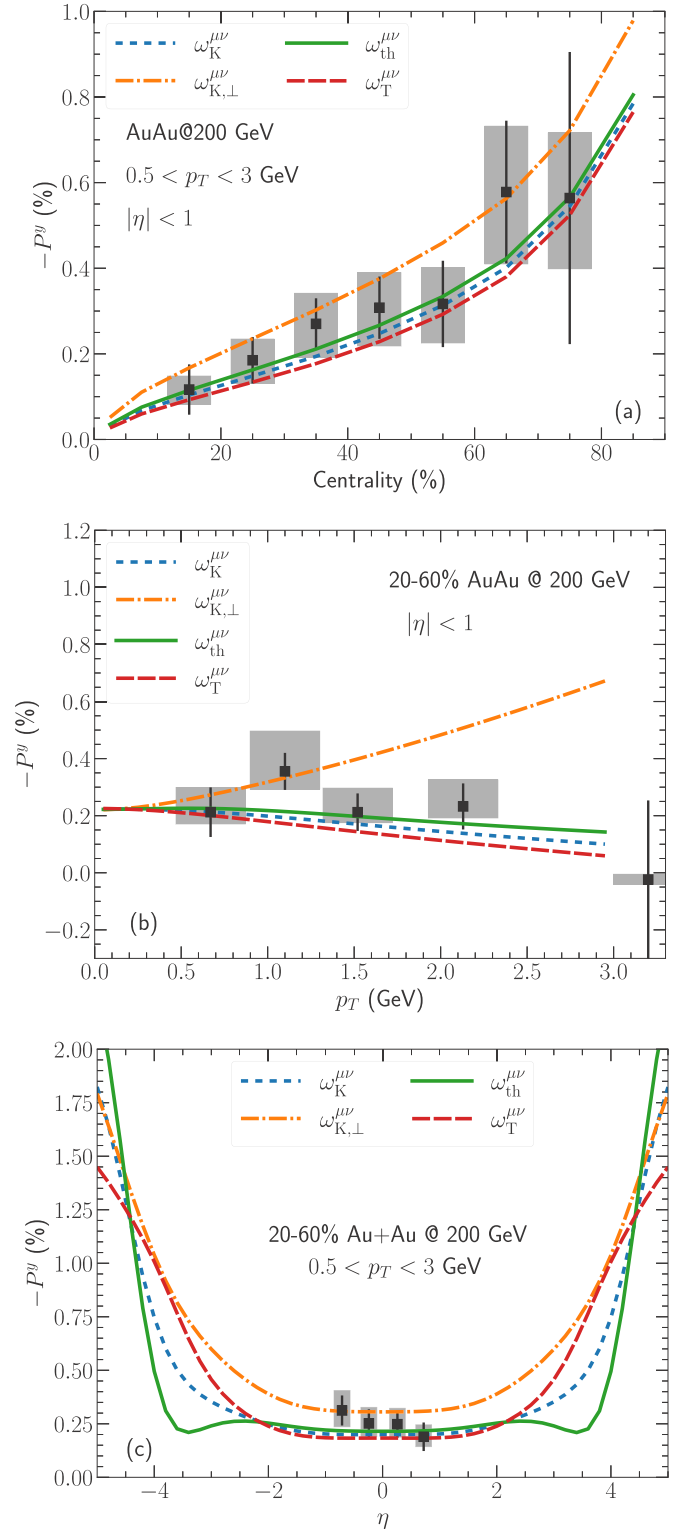


FIG. 11. The global Λ polarization computed with different vorticity tensors with $f = 0.15$ in Au+Au collisions at 200 GeV compared with the STAR measurements [53]. The STAR polarization data points are rescaled by 0.877 because of the latest hyperon decay parameter α_Λ [55].

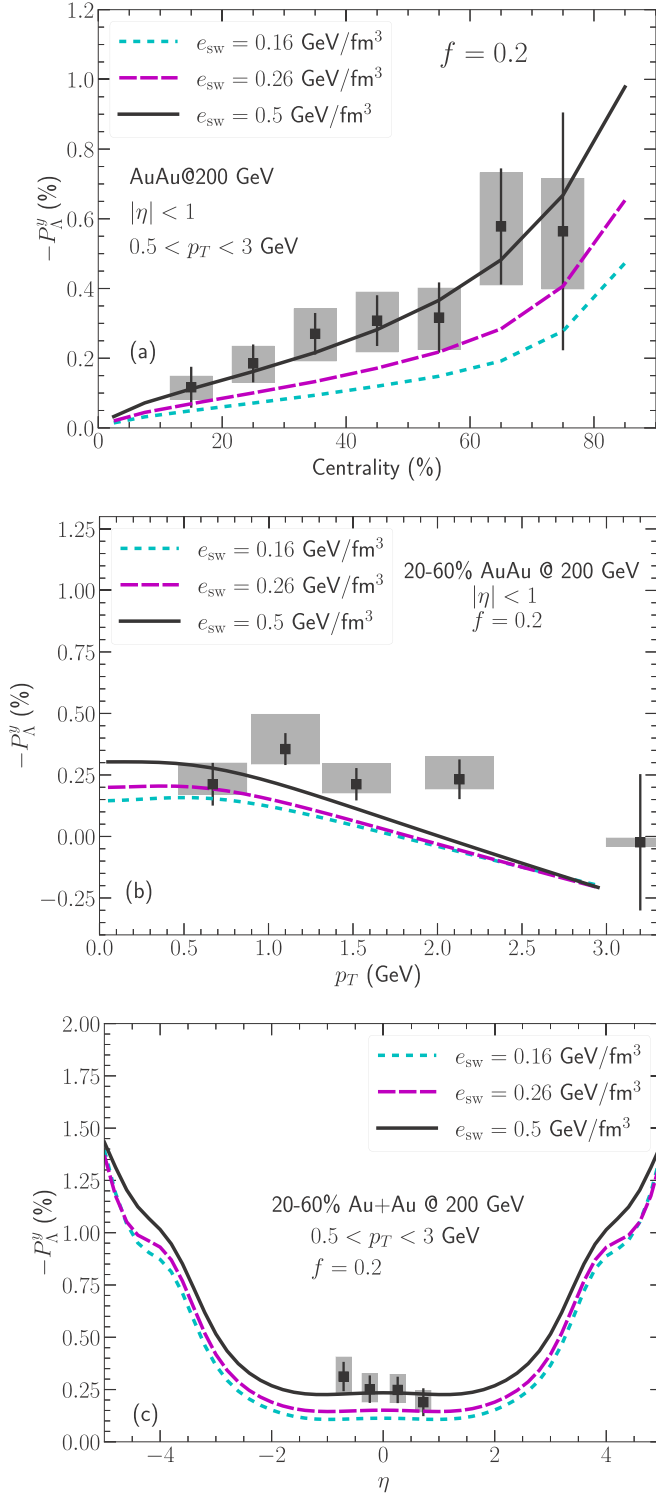


FIG. 12. The global Λ polarization's dependence on the switching energy density in Au+Au collisions at 200 GeV compared with the STAR measurements [53]. The STAR polarization data points are rescaled by 0.877 because of the latest hyperon decay parameter α_{Λ} [55].

T vorticity tensors give very close results of P_{Λ}^y as functions of centrality, p_T , and pseudorapidity within $|\eta| < 2$. These results mean that the temperature gradients do not generate a significant contribution to the azimuthally integrated global polarization. The transverse kinematic vorticity differs from the kinematic vorticity by the fluid acceleration, as shown in Eq. (31). The difference between the results from these two vorticity tensors shows that the fluid acceleration suppresses the overall magnitude of global polarization by $\approx 40\%$. This suppression grows with p_T , as shown in Fig. 11(b).

APPENDIX B: THE FREEZE-OUT ENERGY DENSITY DEPENDENCE ON Λ 'S GLOBAL POLARIZATION

In hydrodynamic plus hadronic transport models, the spin polarizations of Λ and $\bar{\Lambda}$ hyperons are often computed at the particlization hypersurface but not at kinetic freeze-out because it is difficult to track and model the spin information in the microscopic hadronic transport models. In this Appendix, we explore the sensitivity of the Λ 's global polarization on the particlization energy density of the hypersurface.

Figure 12 shows how the global Λ polarization depends on the switching energy density. The overall magnitudes of the global polarization of Λ decrease with the e_{sw} , which is the consequence of smaller fluid gradients on the switching hypersurface with lower e_{sw} . The gradients of temperature and flow velocity decrease roughly as $1/\tau$ at late time of the hydrodynamic evolution [58]. Because the fireball lives longer with a lower switching energy density, the magnitudes of thermal vorticity tensors decrease with e_{sw} , as indicated in Fig. 2.

Figure 12(a) shows that the P_{Λ}^y as function of centrality is 5–10% smaller with the smaller e_{sw} . In addition to the overall suppression, the shape of $P_{\Lambda}^y(p_T)$ gets flatter at lower switching energy density as shown in Fig. 12(b). The change in the p_T dependence is caused by a larger radial flow as the fireball evolves longer to the lower e_{sw} hypersurface. The stronger radial flow blueshifts more Λ to high p_T , flattening the $P_{\Lambda}^y(p_T)$. Finally, Fig. 12(c) shows that a lower e_{sw} hypersurface results in an overall suppression of $P_{\Lambda}^y(\eta)$ with the η -dependence roughly unchanged.

- [1] L. Adamczyk *et al.* (STAR Collaboration), Global Λ hyperon polarization in nuclear collisions: Evidence for the most vortical fluid, *Nature (London)* **548**, 62 (2017).
- [2] Z.-T. Liang and X.-N. Wang, Globally Polarized Quark-Gluon Plasma in Noncentral $A + A$ collisions, *Phys. Rev. Lett.* **94**, 102301 (2005); **96**, 039901(E) (2006).
- [3] F. Becattini, V. Chandra, L. Del Zanna, and E. Grossi, Relativistic distribution function for particles with spin at local thermodynamical equilibrium, *Ann. Phys. (NY)* **338**, 32 (2013).
- [4] F. Becattini, I. Karpenko, M. A. Lisa, I. Upsal, and S. A. Voloshin, Global hyperon polarization at local thermodynamic equilibrium with vorticity, magnetic field, and feed-down, *Phys. Rev. C* **95**, 054902 (2017).
- [5] I. Karpenko and F. Becattini, Study of Λ polarization in relativistic nuclear collisions at $\sqrt{s_{NN}} = 7.7\text{--}200$ GeV, *Eur. Phys. J. C* **77**, 213 (2017).
- [6] Y. Xie, D. Wang, and L. P. Csernai, Global Λ polarization in high energy collisions, *Phys. Rev. C* **95**, 031901(R) (2017).
- [7] I. Karpenko, Vorticity and polarization in heavy ion collisions: Hydrodynamic models, [arXiv:2101.04963](https://arxiv.org/abs/2101.04963).
- [8] X.-G. Huang, Vorticity and spin polarization—A theoretical perspective, *Nucl. Phys. A* **1005**, 121752 (2021).
- [9] F. Becattini and M. A. Lisa, Polarization and vorticity in the quark-gluon plasma, *Annu. Rev. Nucl. Part. Sci.* **70**, 395 (2020).
- [10] X.-G. Huang, J. Liao, Q. Wang, and X.-L. Xia, Vorticity and spin polarization in heavy ion collisions: Transport models, [arXiv:2010.08937](https://arxiv.org/abs/2010.08937).
- [11] F. Becattini, Polarization in relativistic fluids: A quantum field theoretical derivation, in *Strongly Interacting Matter under Rotation*, edited by F. Becattini, J. Liao, and M. Lisa, Lecture Notes in Physics Vol. 987 (Springer, Cham, 2021), pp. 15–52.
- [12] M. A. Lisa, J. G. P. Barbon, D. D. Chinellato, W. M. Serenone, C. Shen, J. Takahashi, and G. Torrieri, Vortex rings from high energy central $p + A$ collisions, *Phys. Rev. C* **104**, L011901 (2021).
- [13] W. M. Serenone, J. G. P. Barbon, D. D. Chinellato, M. A. Lisa, C. Shen, J. Takahashi, and G. Torrieri, Λ polarization from thermalized jet energy, *Phys. Lett. B* **820**, 136500 (2021).
- [14] F. Becattini, J. Liao, and M. Lisa, Strongly interacting matter under rotation: An introduction, in *Strongly Interacting Matter under Rotation*, edited by F. Becattini, J. Liao, and M. Lisa, Lecture Notes in Physics Vol. 987 (Springer, Cham, 2021), pp. 1–14.
- [15] Y. Jiang, Z.-W. Lin, and J. Liao, Rotating quark-gluon plasma in relativistic heavy ion collisions, *Phys. Rev. C* **94**, 044910 (2016); **95**, 049904(E) (2017).
- [16] W. Florkowski, B. Friman, A. Jaiswal, and E. Speranza, Relativistic fluid dynamics with spin, *Phys. Rev. C* **97**, 041901(R) (2018).
- [17] K. Hattori, M. Hongo, X.-G. Huang, M. Matsuo, and H. Taya, Fate of spin polarization in a relativistic fluid: An entropy-current analysis, *Phys. Lett. B* **795**, 100 (2019).
- [18] S. Y. F. Liu, Y. Sun, and C. M. Ko, Spin Polarizations in a Covariant Angular-Momentum-Conserved Chiral Transport Model, *Phys. Rev. Lett.* **125**, 062301 (2020).
- [19] K. Fukushima and S. Pu, Spin hydrodynamics and symmetric energy-momentum tensors—A current induced by the spin vorticity—, *Phys. Lett. B* **817**, 136346 (2021).
- [20] Y.-C. Liu and X.-G. Huang, Anomalous chiral transports and spin polarization in heavy-ion collisions, *Nucl. Sci. Technol.* **31**, 56 (2020).
- [21] J.-H. Gao, G.-L. Ma, S. Pu, and Q. Wang, Recent developments in chiral and spin polarization effects in heavy-ion collisions, *Nucl. Sci. Technol.* **31**, 90 (2020).
- [22] S. Shi, C. Gale, and S. Jeon, From chiral kinetic theory to relativistic viscous spin hydrodynamics, *Phys. Rev. C* **103**, 044906 (2021).
- [23] S. Li, M. A. Stephanov, and H.-U. Yee, Nondissipative Second-Order Transport, Spin, and Pseudogauge Transformations in Hydrodynamics, *Phys. Rev. Lett.* **127**, 082302 (2021).
- [24] R. Singh, G. Sophys, and R. Ryblewski, Spin polarization dynamics in the Gubser-expanding background, *Phys. Rev. D* **103**, 074024 (2021).
- [25] F. Becattini and Iu. Karpenko, Collective Longitudinal Polarization in Relativistic Heavy-Ion Collisions at Very High Energy, *Phys. Rev. Lett.* **120**, 012302 (2018).
- [26] X.-L. Xia, H. Li, Z.-B. Tang, and Q. Wang, Probing vorticity structure in heavy-ion collisions by local Λ polarization, *Phys. Rev. C* **98**, 024905 (2018).
- [27] W. Florkowski, A. Kumar, A. Mazeliauskas, and R. Ryblewski, Longitudinal spin polarization in a thermal model, *Phys. Rev. C* **100**, 054907 (2019).
- [28] H.-Z. Wu, L.-G. Pang, X.-G. Huang, and Q. Wang, Local spin polarization in high energy heavy ion collisions, *Phys. Rev. Research* **1**, 033058 (2019).
- [29] F. Becattini, G. Cao, and E. Speranza, Polarization transfer in hyperon decays and its effect in relativistic nuclear collisions, *Eur. Phys. J. C* **79**, 741 (2019).
- [30] S. A. Crooker and D. L. Smith, Imaging Spin Flows in Semiconductors Subject to Electric, Magnetic, and Strain Fields, *Phys. Rev. Lett.* **94**, 236601 (2005).
- [31] A. G. Mal'shukov, C. S. Tang, C. S. Chu, and K. A. Chao, Strain-Induced Coupling of Spin Current to Nanomechanical Oscillations, *Phys. Rev. Lett.* **95**, 107203 (2005).
- [32] Y. Hidaka, S. Pu, and D.-L. Yang, Nonlinear responses of chiral fluids from kinetic theory, *Phys. Rev. D* **97**, 016004 (2018).
- [33] S. Y. F. Liu and Y. Yin, Spin Hall effect in heavy-ion collisions, *Phys. Rev. D* **104**, 054043 (2021).
- [34] S. Y. F. Liu and Y. Yin, Spin polarization induced by the hydrodynamic gradients, *J. High Energy Phys.* **07** (2021) 188.
- [35] F. Becattini, M. Buzzegoli, and A. Palermo, Spin-thermal shear coupling in a relativistic fluid, *Phys. Lett. B* **820**, 136519 (2021).
- [36] B. Fu, S. Y. F. Liu, L. Pang, H. Song, and Y. Yin, Shear-Induced Spin Polarization in Heavy-Ion Collisions, *Phys. Rev. Lett.* **127**, 142301 (2021).
- [37] F. Becattini, M. Buzzegoli, A. Palermo, G. Inghirami, and I. Karpenko, Local polarization and isothermal local equilibrium in relativistic heavy ion collisions, [arXiv:2103.14621](https://arxiv.org/abs/2103.14621).
- [38] C. Yi, S. Pu, and D.-L. Yang, Revisit local spin polarization beyond global equilibrium in relativistic heavy ion collisions, [arXiv:2106.00238](https://arxiv.org/abs/2106.00238).
- [39] C. Shen and S. Alzhirani, Collision-geometry-based 3D initial condition for relativistic heavy-ion collisions, *Phys. Rev. C* **102**, 014909 (2020).
- [40] C. Shen and B. Schenke, Dynamical initial state model for relativistic heavy-ion collisions, *Phys. Rev. C* **97**, 024907 (2018).
- [41] C. W. Misner, K. S. Thorne, and J. A. Wheeler, *Gravitation* (W. H. Freeman, San Francisco, 1973).
- [42] T. Hirano, U. W. Heinz, D. Kharzeev, R. Lacey, and Y. Nara, Hadronic dissipative effects on elliptic flow in ultrarelativistic heavy-ion collisions, *Phys. Lett. B* **636**, 299 (2006).

- [43] G. S. Denicol, C. Gale, S. Jeon, A. Monnai, B. Schenke, and C. Shen, Net baryon diffusion in fluid dynamic simulations of relativistic heavy-ion collisions, *Phys. Rev. C* **98**, 034916 (2018).
- [44] B. Schenke, S. Jeon, and C. Gale, (3+1)D hydrodynamic simulation of relativistic heavy-ion collisions, *Phys. Rev. C* **82**, 014903 (2010).
- [45] B. Schenke, S. Jeon, and C. Gale, Higher flow harmonics from (3+1)D event-by-event viscous hydrodynamics, *Phys. Rev. C* **85**, 024901 (2012).
- [46] J.-F. Paquet, C. Shen, G. S. Denicol, M. Luzum, B. Schenke, S. Jeon, and C. Gale, Production of photons in relativistic heavy-ion collisions, *Phys. Rev. C* **93**, 044906 (2016).
- [47] The official website of MUSIC, <https://www.physics.mcgill.ca/music>. The latest version of the code can be downloaded from <https://github.com/MUSIC-fluid/MUSIC>.
- [48] A. Monnai, B. Schenke, and C. Shen, Equation of state at finite densities for QCD matter in nuclear collisions, *Phys. Rev. C* **100**, 024907 (2019).
- [49] G. S. Denicol, H. Niemi, E. Molnar, and D. H. Rischke, Derivation of transient relativistic fluid dynamics from the Boltzmann equation, *Phys. Rev. D* **85**, 114047 (2012); **91**, 039902(E) (2105).
- [50] G. S. Denicol, S. Jeon, and C. Gale, Transport coefficients of bulk viscous pressure in the 14-moment approximation, *Phys. Rev. C* **90**, 024912 (2014).
- [51] L. Adamczyk *et al.* (STAR Collaboration), Harmonic decomposition of three-particle azimuthal correlations at energies available at the BNL Relativistic Heavy Ion Collider, *Phys. Rev. C* **98**, 034918 (2018).
- [52] D. Oliinychenko, C. Shen, and V. Koch, Deuteron production in AuAu collisions at $\sqrt{s_{NN}}=7\text{--}200$ GeV via pion catalysis, *Phys. Rev. C* **103**, 034913 (2021).
- [53] J. Adam *et al.* (STAR Collaboration), Global polarization of Λ hyperons in Au+Au collisions at $\sqrt{s_{NN}}=200$ GeV, *Phys. Rev. C* **98**, 014910 (2018).
- [54] L. Adamczyk *et al.* (STAR Collaboration), Beam-Energy Dependence of the Directed Flow of Protons, Antiprotons, and Pions in Au+Au Collisions, *Phys. Rev. Lett.* **112**, 162301 (2014).
- [55] P. A. Zyla *et al.* (Particle Data Group), Review of particle physics, *Prog. Theor. Exp. Phys.* **2020**, 083C01 (2020).
- [56] O. Vitiuk, L. V. Bravina, and E. E. Zabrodin, Is different Λ and $\bar{\Lambda}$ polarization caused by different spatio-temporal freeze-out picture? *Phys. Lett. B* **803**, 135298 (2020).
- [57] J. Adam *et al.* (STAR Collaboration), Polarization of Λ ($\bar{\Lambda}$) Hyperons Along the Beam Direction in Au+Au Collisions at $\sqrt{s_{NN}}=200$ GeV, *Phys. Rev. Lett.* **123**, 132301 (2019).
- [58] G. Vujanovic, J.-F. Paquet, C. Shen, G. S. Denicol, S. Jeon, C. Gale, and U. Heinz, Exploring the influence of bulk viscosity of QCD on dilepton tomography, *Phys. Rev. C* **101**, 044904 (2020).